PHYSICAL REVIEW B **85**, 134107 (2012)

High-resolution spectroscopy of single NV defects coupled with nearby ^{13}C nuclear spins in diamond

A. Dréau,[1] J.-R. Maze,[2] M. Lesik,[3] J.-F. Roch,[3] and V. Jacques[1,*]

[1]*Laboratoire de Photonique Quantique et Moléculaire, Ecole Normale Supérieure de Cachan and CNRS UMR 8537, 94235 Cachan, France*

[2]*Facultad de Física, Pontificia Universidad Católica de Chile, Santiago 7820436, Chile*

[3]*Laboratoire Aimé Cotton, CNRS UPR 3321 and Université Paris-Sud, 91405 Orsay, France*

(Received 9 February 2012; published 20 April 2012)

We report a systematic study of the hyperfine interaction between the electron spin of a single nitrogen-vacancy (NV) defect in diamond and nearby ^{13}C nuclear spins, by using pulsed electron-spin resonance spectroscopy. We isolate a set of discrete values of the hyperfine coupling strength ranging from 14 MHz to 400 kHz and corresponding to ^{13}C nuclear spins placed at different lattice sites of the diamond matrix. For each lattice site, the hyperfine interaction is further investigated through nuclear-spin polarization measurements and by studying the magnetic field dependence of the hyperfine splitting. This work provides information that is relevant for the development of nuclear-spin-based quantum register in diamond.

DOI: 10.1103/PhysRevB.85.134107 PACS number(s): 76.30.Mi, 33.15.Pw, 76.70.Hb, 42.50.Dv

I. INTRODUCTION

Owing to its outstanding optical and electron-spin properties, the negatively charged nitrogen-vacancy (NV) color center in diamond has recently emerged as a promising candidate for a broad range of applications including quantum information processing (QIP),[1–5] photonic devices,[6–8] hybrid quantum systems,[9–11] nanoscale magnetometry,[12–15] and imaging in life science.[16,17] For QIP applications, coherent interactions of the NV defect with nearby nuclear spins of the diamond lattice provide a fertile resource for the realization of universal quantum gates,[1] quantum registers,[2–4] and multipartite entangled states.[5] For such experiments, individual nuclear spins are read out optically by coherently mapping their states onto the NV defect electron spin, which can be efficiently polarized and read out with a long coherence time, even at room temperature.[18,19]

Two nuclear-spin species commonly interact with the NV defect, namely the intrinsic nitrogen atom of the defect and ^{13}C atoms placed randomly in the diamond lattice. The hyperfine interaction between the NV defect electron spin and its nitrogen atom has been extensively characterized over the last years, both for native NV defects associated with ^{14}N atoms and for implanted NV defects with ^{15}N isotopes.[20] Since the nitrogen nuclear spin occurs deterministically, it could be used as a robust memory qubit for scalable architectures of diamond-based quantum information protocols.[3] In addition, because the nitrogen nuclear spin shares its symmetry axis with the NV defect, single-shot readout measurements can be achieved at room temperature.[21] In contrast, ^{13}C nuclear spins occur randomly in the diamond lattice and can be used as a platform for studying the coherent dynamics of multi-spin systems as well as for increasing the number of qubits in diamond-based quantum registers.

In this paper, we report a systematic study of the hyperfine interaction between single NV defects and individual ^{13}C nuclear spins. Using pulsed-ESR spectroscopy, we analyze the possible hyperfine coupling strengths induced by ^{13}C placed at different lattice sites of the diamond matrix. Excluding the well-known 130 MHz splitting linked to ^{13}C placed in the nearest neighbor lattice sites of the vacancy,[20,22] we focus on lattice sites corresponding to hyperfine splittings ranging from 14 MHz to 400 kHz. For each lattice site, properties of the ^{13}C hyperfine tensor are inferred by using nuclear-spin polarization measurements and by studying the magnetic field dependence of the hyperfine splitting. This work, which completes a recent work by Smeltzer *et al.*,[23] is relevant for the realization of multipartite entangled state among multi-nuclear-spin systems as well as for extending single shot readout measurements recently observed on the ^{14}N nuclear spin.[21]

II. SINGLE NV DEFECTS COUPLED WITH NEARBY NUCLEAR SPINS THROUGH HYPERFINE INTERACTION

A. Experimental arrangement

The negatively charged NV defect in diamond consists of a substitutional nitrogen atom (N) associated with a vacancy (V) in an adjacent lattice site of the diamond matrix. Its ground state is a spin triplet $S = 1$ with an intrinsic spin quantization axis provided by the NV defect symmetry axis (z) and a zero-field splitting $D_{gs} = 2.87$ GHz between $m_s = 0$ and $m_s = \pm 1$ spin sublevels [Fig. 1(a)].[24,25] The excited state is also a spin triplet, associated with a broadband and perfectly photostable red photoluminescence (PL), which enables optical detection of single NV defects using confocal microscopy.[26] Besides, the excited state is an orbital doublet which is averaged at room temperature,[27,28] leading to a zero-field splitting $D_{es} = 1.42$ GHz with the same quantization axis and similar gyromagnetic ratio as in the ground state ($g_e \approx 2$).[29,30] Radiative transition selection rules associated with the spin state quantum number provide a high degree of spin polarization in the $m_s = 0$ sublevel through optical pumping. In addition, the PL intensity is significantly higher when the $m_s = 0$ state is populated, allowing the detection of electron-spin resonances (ESR) on a single NV defect by optical means.[26]

We investigate native NV defects in an ultra-pure synthetic type IIa diamond crystal grown using a microwave-assisted chemical vapor deposition (CVD) process (Element 6). In such a sample with a natural abundance of ^{13}C isotope (1.1%), the typical coherence time T_2^* of the NV defect electron spin is on the order of a few μs, corresponding to an inhomogeneous dephasing rate γ_2^* on the order of a few hundreds of kHz.[18,19]

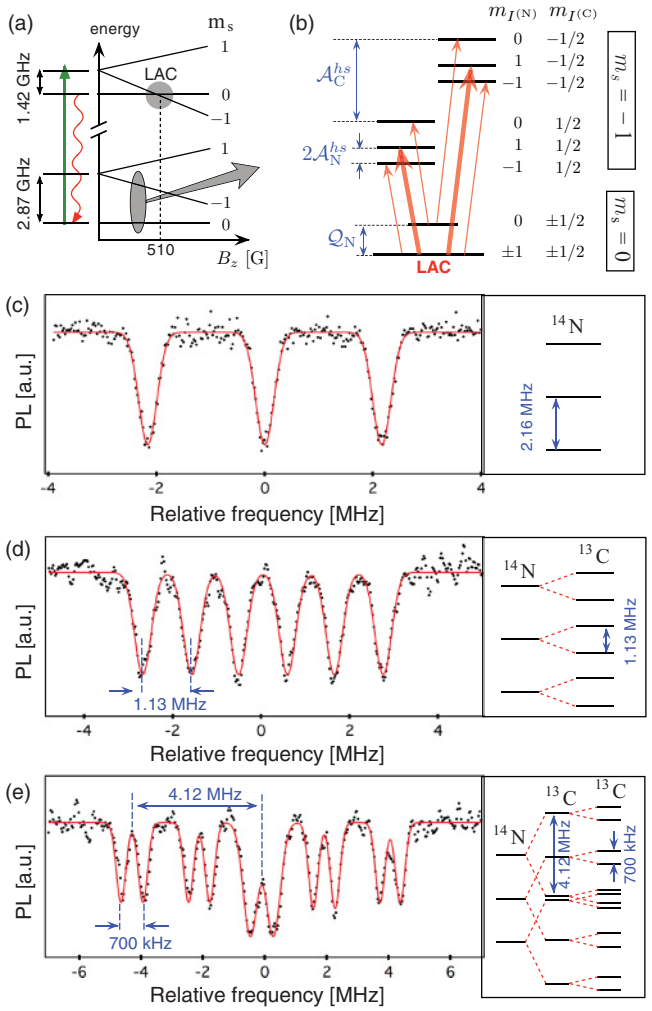

FIG. 1. (Color online) (a) Energy-level diagram of the NV defect as a function of the amplitude of a static magnetic field B applied along the NV defect axis. (b) Hyperfine structure of the $m_s = 0$ and $m_s = -1$ ground-state manifolds for a NV defect coupled to its ^{14}N (nuclear-spin projection $m_{I^{(N)}}$) and a single ^{13}C (nuclear-spin projection $m_{I^{(C)}}$). The energy level scheme is given for a positive ^{13}C hyperfine splitting, i.e., $\mathcal{A}_{zz} > 0$, and considering that off-diagonal components of the ^{13}C hyperfine tensor are negligible. ESR spectra exhibit six nuclear-spin conserving transitions (red arrows). All notations are defined in the main text. (c)–(e) ESR spectra recorded for a single NV defect coupled to its ^{14}N and (c) zero, (d) one, and (e) two nearby ^{13}C. The blue values indicate the corresponding hyperfine splittings and solid lines are data fit with Gaussian functions. For this experiment, a magnetic field $B \approx 20$ G is applied along the NV defect axis in order to lift the degeneracy of the $m_s = \pm 1$ electron-spin sublevels. For a magnetic field amplitude $B \approx 510$ G, a level anticrossing (LAC) in the excited-state [highlighted in (a)] induces nuclear-spin polarization such that only two nuclear-spin conserving transitions are observed, as indicated with bold arrows in (b) (see Fig. 5).

Individual NV defects are optically addressed at room temperature using a confocal microscope combined with a photon-counting detection system. A permanent magnet is used to apply a static magnetic field along the NV defect axis, while ESR transitions are driven with a microwave field applied through a copper microwire directly spanned on the diamond surface. High-resolution ESR spectroscopy of single NV defects coupled by hyperfine interaction with nearby ^{13}C nuclear spins is achieved through repetitive excitation of the NV defect with a resonant microwave π-pulse followed by a 300-ns readout laser pulse.[31] ESR spectra are recorded by continuously repeating this sequence while sweeping the π-pulse frequency and recording the PL intensity. Owing to spin-dependent PL of the NV defect, ESR is evidenced as a drop of the PL signal [Fig. 1(c)]. For all the experiments, the microwave power is adjusted in order to set the π-pulse duration between 2 and 3 μs, as verified by recording electron-spin Rabi oscillations. The π-pulse duration is thus on the order of the NV defect electron-spin coherence time. In this situation, the ESR profile is Gaussian and its linewidth is given by the inhomogeneous dephasing rate γ_2^* of the NV defect electron spin, since power broadening is fully canceled in the measurement.[31]

B. Spin Hamiltonian

We consider single NV defects associated with native ^{14}N isotopes (99.6% abundance), corresponding to a nuclear spin $I^{(N)} = 1$. For a magnetic field B applied along the NV defect axis, the ground-state spin Hamiltonian in frequency unit reads as

$$\mathcal{H}_0 = D_{gs}\hat{S}_z^2 + \gamma_e B\hat{S}_z + \gamma_n^{(N)} B\hat{I}_z^{(N)} + \mathcal{Q}_N\left(\hat{I}_z^{(N)}\right)^2 + \hat{\mathbf{S}}\cdot\mathcal{A}_N\cdot\hat{\mathbf{I}}^{(N)}, \quad (1)$$

where $\mathcal{Q}_N = -5.01$ MHz is the ^{14}N quadrupole splitting,[20] $\mathcal{A}_N$ its hyperfine tensor, and γ_e (resp. $\gamma_n^{(N)}$) is the electron-spin (resp. ^{14}N nuclear spin) gyromagnetic ratio. The ^{14}N hyperfine tensor has been extensively characterized over the last years and leads to a splitting of $\mathcal{A}_N^{hs} = -2.16$ MHz between ESR frequencies associated with different ^{14}N nuclear-spin projections.[32] For single NV defects without any strongly coupled ^{13}C nuclear spins, the ESR spectrum thus always exhibit three hyperfine lines [Figs. 1(b) and 1(c)].

When a neighboring lattice site of the NV defect is occupied by a ^{13}C isotope, corresponding to a nuclear spin $I^{(C)} = 1/2$, the spin Hamiltonian becomes

$$\mathcal{H} = \mathcal{H}_0 + \gamma_n B\hat{I}_z^{(C)} + \hat{\mathbf{S}}\cdot\mathcal{A}_C\cdot\hat{\mathbf{I}}^{(C)}, \quad (2)$$

where γ_n is the gyromagnetic ratio of the ^{13}C nuclear spin and $\mathcal{A}_C$ its hyperfine tensor defined by

$$\mathcal{A}_C = \begin{pmatrix} \mathcal{A}_{xx} & \mathcal{A}_{xy} & \mathcal{A}_{xz} \\ \mathcal{A}_{yx} & \mathcal{A}_{yy} & \mathcal{A}_{yz} \\ \mathcal{A}_{zx} & \mathcal{A}_{zy} & \mathcal{A}_{zz} \end{pmatrix}. \quad (3)$$

In the secular approximation, i.e., neglecting $\hat{S}_x$ and $\hat{S}_y$ terms, this Hamiltonian simplifies as

$$\mathcal{H} = \mathcal{H}_0 + \gamma_n B\hat{I}_z^{(C)} + \hat{S}_z\sum_i \mathcal{A}_{zi}\hat{I}_i^{(C)}. \quad (4)$$

For clarity purposes, we restrict the study to the $m_s = 0$ and $m_s = -1$ electronic spin manifolds with a fixed ^{14}N nuclear-spin projection, e.g., $m_{I^{(N)}} = +1$. All the results are identical while considering the two other ^{14}N nuclear-spin projections. In the basis $\{|m_s, m_{I^{(C)}}\rangle\} = \{|0,\tfrac{1}{2}\rangle; |0,-\tfrac{1}{2}\rangle; |-1,\tfrac{1}{2}\rangle; |-1,-\tfrac{1}{2}\rangle\}$

and considering $\mathcal{A}_{zz} > 0$, the Hamiltonian described by equation (4) can be written as

$$\mathcal{H} = \begin{bmatrix} \frac{\gamma_n B}{2} & 0 & 0 & 0 \\ 0 & -\frac{\gamma_n B}{2} & 0 & 0 \\ 0 & 0 & \Sigma - \frac{\mathcal{A}_{zz}-\gamma_n B}{2} & -\frac{\mathcal{A}_{\rm nd}}{2} e^{-i\phi} \\ 0 & 0 & -\frac{\mathcal{A}_{\rm nd}}{2} e^{i\phi} & \Sigma + \frac{\mathcal{A}_{zz}-\gamma_n B}{2} \end{bmatrix}, \quad (5)$$

where

$$\begin{aligned} \mathcal{A}_{\rm nd} &= \sqrt{\mathcal{A}_{xz}^2 + \mathcal{A}_{yz}^2} \\ \Sigma &= D_{gs} - \gamma_e B - \mathcal{A}_N^{hs} \\ \tan\phi &= \frac{\mathcal{A}_{yz}}{\mathcal{A}_{xz}}. \end{aligned} \quad (6)$$

We note that the ^{14}N nuclear Zeeman splitting and the ^{14}N quadrupole splitting are ignored in Eq. (5) since they only introduce a global shift of the energy levels. In this framework, the eigenenergies of the NV defect electron spin coupled by hyperfine interaction with a single ^{13}C nuclear spin are given by

$$\nu_1 = +\frac{\gamma_n B}{2} \quad (7)$$

$$\nu_2 = -\frac{\gamma_n B}{2} \quad (8)$$

$$\nu_3 = \Sigma - \frac{1}{2}\sqrt{\mathcal{A}_{\rm nd}^2 + (\mathcal{A}_{zz} - \gamma_n B)^2} \quad (9)$$

$$\nu_4 = \Sigma + \frac{1}{2}\sqrt{\mathcal{A}_{\rm nd}^2 + (\mathcal{A}_{zz} - \gamma_n B)^2}, \quad (10)$$

and the associated eigenstates can be written as

$$\begin{aligned} |\psi_1\rangle &= \left|0, \frac{1}{2}\right\rangle \\ |\psi_2\rangle &= \left|0, -\frac{1}{2}\right\rangle \\ |\psi_3\rangle &= |+\rangle = \cos\left(\frac{\theta}{2}\right)\left|-1, \frac{1}{2}\right\rangle + \sin\left(\frac{\theta}{2}\right)e^{i\phi}\left|-1, -\frac{1}{2}\right\rangle \\ |\psi_4\rangle &= |-\rangle = -\sin\left(\frac{\theta}{2}\right)e^{-i\phi}\left|-1, \frac{1}{2}\right\rangle + \cos\left(\frac{\theta}{2}\right)\left|-1, -\frac{1}{2}\right\rangle \end{aligned}$$

where

$$\tan\theta = \frac{\mathcal{A}_{\rm nd}}{\mathcal{A}_{zz} - \gamma_n B}. \quad (11)$$

Allowed (T_{13}, T_{24}) and forbidden (T_{14}, T_{23}) electron-spin transition frequencies are therefore given by

$$T_{13} = \Sigma - \frac{1}{2}\sqrt{\mathcal{A}_{\rm nd}^2 + (\mathcal{A}_{zz} - \gamma_n B)^2} - \frac{\gamma_n B}{2} \quad (12)$$

$$T_{24} = \Sigma + \frac{1}{2}\sqrt{\mathcal{A}_{\rm nd}^2 + (\mathcal{A}_{zz} - \gamma_n B)^2} + \frac{\gamma_n B}{2} \quad (13)$$

$$T_{14} = \Sigma + \frac{1}{2}\sqrt{\mathcal{A}_{\rm nd}^2 + (\mathcal{A}_{zz} - \gamma_n B)^2} - \frac{\gamma_n B}{2} \quad (14)$$

$$T_{23} = \Sigma - \frac{1}{2}\sqrt{\mathcal{A}_{\rm nd}^2 + (\mathcal{A}_{zz} - \gamma_n B)^2} + \frac{\gamma_n B}{2}, \quad (15)$$

where the numbering is determined by the corresponding energy levels, $T_{ik} = \nu_k - \nu_i$.

If $|\mathcal{A}_{zz} - \gamma_n B|$ and $\mathcal{A}_{\rm nd}$ have the same order of magnitude, four electron-spin transitions can thus be observed for each ^{14}N nuclear-spin projection, with a relative intensity between forbidden and allowed transitions given by $\tan^2(\frac{\theta}{2})$. When $\mathcal{A}_{zz} = \gamma_n B$, i.e., when $\theta = \pi/2$, the amplitudes of allowed and forbidden electron-spin transitions are identical. This particular case is experimentally observed and analyzed in Sec. III B (Figs. 3 and 4).

In the limit where $|\mathcal{A}_{zz} - \gamma_n B| \gg \mathcal{A}_{\rm nd}$, i.e., when the angle θ approaches zero,

$$\begin{aligned} |\psi_1\rangle &= \left|0, \tfrac{1}{2}\right\rangle \\ |\psi_2\rangle &= \left|0, -\tfrac{1}{2}\right\rangle \\ |\psi_3\rangle &= \left|-1, \tfrac{1}{2}\right\rangle \\ |\psi_4\rangle &= \left|-1, -\tfrac{1}{2}\right\rangle. \end{aligned}$$

In this situation, the ^{13}C nuclear-spin projection along the NV defect axis is identical in the $m_s = 0$ and $m_s = -1$ electronic spin manifolds and only two nuclear-spin conserving transitions can be observed (T_{13} and T_{24}). By considering all the ^{14}N nuclear-spin projections, the ESR spectrum thus exhibits six nuclear-spin conserving transitions as schematically depicted in Fig. 1(b).

III. EXPERIMENTAL OBSERVATIONS

A. Low magnetic field hyperfine splittings

We first study the possible values of hyperfine splittings induced by nearby ^{13}C nuclear spins for a low magnetic field magnitude ($B \approx 20$ G) applied along the NV defect axis. In this condition, the nuclear Zeeman term can be neglected ($T_{13} = T_{23}$, $T_{24} = T_{14}$) and the ^{13}C hyperfine interaction leads to a splitting

$$\mathcal{A}_{\rm C}^{hs}(@20\ {\rm G}) = T_{24} - T_{13} = \pm\sqrt{\mathcal{A}_{\rm nd}^2 + \mathcal{A}_{zz}^2}$$

between ESR frequencies associated with different ^{13}C nuclear-spin projections, with a sign given by the one of the $\mathcal{A}_{zz}$ component [Fig. 1(b)].

A systematic study of the ^{13}C hyperfine coupling strength was realized by performing pulsed-ESR spectroscopy on a set of roughly 400 single NV defects. Even though most of the ESR spectra only show the three hyperfine lines linked to the ^{14}N nuclear spin [Fig. 1(c)], the subset ($\approx$25%) of NV defects strongly coupled to one (resp. two) ^{13}C nuclear spin exhibit six (resp. twelve) resonance lines [Figs. 1(d) and 1(e)]. From each ESR spectrum, the hyperfine splitting between the ^{13}C manifolds was extracted from a fit with Gaussian functions, constrained to have the same linewidth and amplitude, and with a fixed splitting between ^{14}N hyperfine lines ($\mathcal{A}_{\rm N}^{\rm hs} = -2.16$ MHz).

As shown in Fig. 2, the ^{13}C hyperfine splittings are distributed over a set of discrete values corresponding to different lattice sites of the diamond matrix. Following the notations introduced in Ref. 23, hyperfine splittings such that $\mathcal{A}_{\rm C}^{hs} > 2$ MHz are labeled from A to H, corresponding to possible lattice sites inferred from *ab initio* calculations.[33,34]

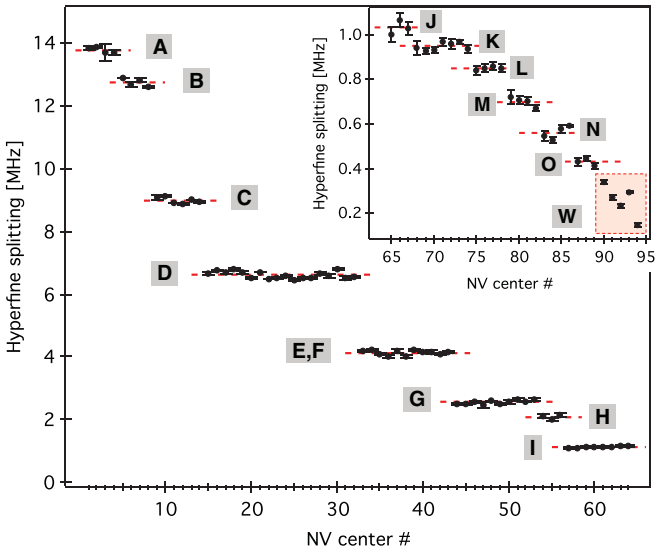

FIG. 2. (Color online) Distribution of ^{13}C hyperfine splittings observed for a set of roughly 400 single NV defects at low magnetic field ($B \approx 20$ G). The well-documented[20,22] 130 MHz splitting linked to a ^{13}C placed in the nearest neighbor lattice sites of the vacancy is not represented. The capital letters denote the lattice sites corresponding to a given hyperfine splitting. The dashed red lines represent the mean value of each ^{13}C family (A to O) and error bars represent estimated errors in ESR spectra fit with a 95% confidence interval. For a given ^{13}C family, the small dispersion of the hyperfine splittings is attributed to local paramagnetic defects, which could shift the nuclear-spin levels. The mean of the hyperfine splitting associated with each ^{13}C family are summarized in Table I.

Smaller hyperfine splittings are arbitrarily denoted from I to O, but no correspondence with a specific lattice site of the diamond matrix is currently available, since the accuracy of *ab initio* calculation is hardly better than a few hundred kHz. We note that ^{13}C families are sorted according to the strength of the hyperfine coupling and by their polarization response at the excited-state level anticrossing (LAC), as analyzed in details in Sec. III C.

For a few single NV defects, the inhomogeneous dephasing rate γ_2^* was small enough to detect hyperfine splittings below 300 kHz, labeled W in Fig. 2. Within our statistic, it is not possible to clearly identify common lattice sites for such weak couplings. However, the possible discrete values of the hyperfine splittings should reach a quasicontinuum when the ^{13}C is placed far away from the NV defect because many different lattice sites might exhibit similar hyperfine coupling strengths. A more systematic study of weaker ^{13}C hyperfine splittings could be pursued by using a CVD-grown diamond isotopically enriched with ^{12}C atoms, in which the inhomogeneous dephasing rate of the NV defect electron spin can reach a few tens of kHz.[18,19] The drawback would obviously be a lower rate of detection of ^{13}C nuclear spin per single NV defect.

The mean of the hyperfine splitting associated with each ^{13}C family is summed up in Table I. We note that for families A to G, the results are in good agreement with recent single site measurements.[23]

TABLE I. Summary of hyperfine splittings $\mathcal{A}_C^{hs}$ measured at $B = 20$ G and at $B = 510$ G. The last column indicates for each ^{13}C family the polarization efficiency $\mathcal{P}$ measured at the excited-state LAC using pulsed-ESR spectrocopy, i.e., with an optical pumping duration of 300 ns. Numbers between parenthesis indicate the standard deviation on the last digit for a number of NV centers that is given between square brackets.

^{13}C family	$\mathcal{A}_C^{hs}$(@ 20 G) [MHz]	$\mathcal{A}_C^{hs}$(@ 510 G) [MHz]	$\mathcal{P}$ [%]
A	13.78 (9) [4]	13.69 (5) [3]	52 (20) [3]
B	12.8 (1) [4]	12.73 (1) [3]	53 (13) [3]
C	− 9.0 (1) [6]	− 8.9 (2) [4]	− 56 (8) [4]
D	− 6.6 (1) [18]	− 6.55 (2) [6]	− 65 (10) [6]
E, F	4.12 (8) [11]	4.21 (8) [3]	43 (6) [3]
G	2.55 (6) [10]	2.54 (3) [4]	34 (6) [4]
H	2.09 (8) [3]	2.15 (4) [3]	54 (4) [3]
I	1.13 (2) [8]	1.20 (6) [2]	0 (1) [2]
J	− 1.03 (3) [3]	− 0.99 (1) [2]	− 3 (1) [2]
K	0.95 (2) [7]	0.92 (7) [3]	60 (8) [3]
L	0.85 (1) [4]	0.86 (3) [3]	1 (1) [3]
M	− 0.70 (3) [4]	− 0.69 (2) [3]	− 4 (4) [3]
N	0.56 (3) [4]	0.52 (2) [2]	2 (4) [2]
O	0.43 (2) [3]	0.40 (2) [3]	13 (7) [3]

B. Effect of off-diagonal components of the hyperfine tensor

With the aim of observing the effects of anisotropic components of the hyperfine tensor, the ^{13}C coupling strengths were first measured while applying a magnetic field near $B = 510$ G along the NV defect axis. In this situation, the hyperfine splitting between allowed electron-spin transitions (T_{13} and T_{24}) is given by

$$\mathcal{A}_C^{hs}(@510\text{ G}) = \sqrt{\mathcal{A}_{nd}^2 + (\mathcal{A}_{zz} - \gamma_n B)^2} + \gamma_n B.$$

As summarized in Table I, most ^{13}C hyperfine splittings are identical within the error bars at low and high magnetic fields. However, for some ^{13}C lattice sites, e.g., for families E and I, their relative differences becomes significant, which is an indication that anisotropic components of the hyperfine tensor lead to a different nuclear-spin projection along the NV defect axis in the $m_s = 0$ and $m_s = -1$ electronic spin manifolds.

In the limit where the components $|\mathcal{A}_{zz} - \gamma_n B|$ and $\mathcal{A}_{nd}$ reach the same order of magnitude, forbidden electron-spin transitions (T_{14} and T_{23}) can even be identified in the ESR spectrum. This situation is observed for single NV defects coupled with ^{13}C belonging to family I, as depicted in Fig. 3. At low magnetic field, since $T_{13} = T_{23}$ and $T_{24} = T_{14}$, only two ^{13}C hyperfine transitions can be observed for each ^{14}N nuclear-spin projection [Fig. 3(a)]. When the magnetic field magnitude increases, forbidden transitions appears in the ESR spectrum [Figs. 3(b) and 3(c)]. The frequencies of forbidden and allowed electron-spin transitions were measured as a function of the magnetic field magnitude [Fig. 4(a)]. Data fitting with Eqs. (12)–(15) allows us to extract $\mathcal{A}_{zz} = 1.02$ (2) MHz and $\mathcal{A}_{nd} = 0.51$ (2) MHz. In addition, plotting $T_{23} - T_{13}$ as a function of the magnetic field allows measurement of the ^{13}C nuclear-spin gyromagnetic ratio $\gamma_n = 1.07$ (1) kHz.G^{-1}

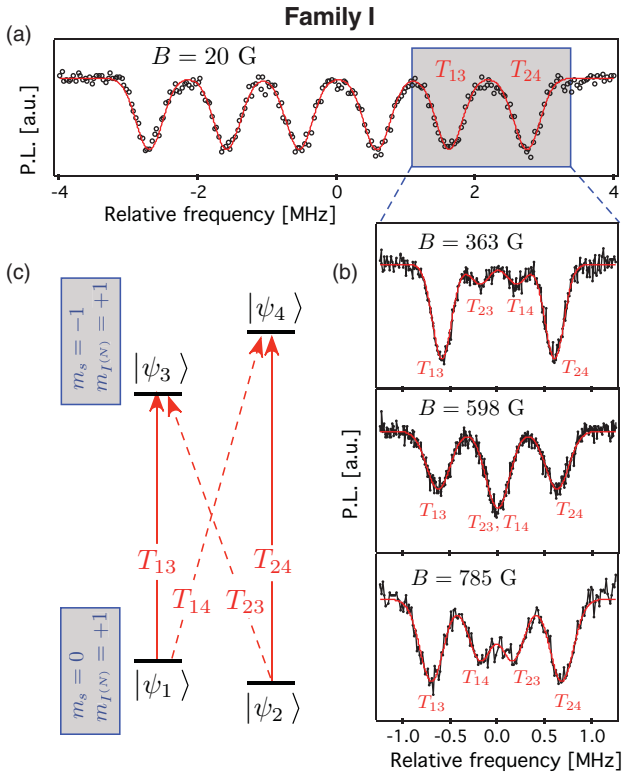

FIG. 3. (Color online) (a) Typical ESR spectrum recorded at low magnetic field ($B = 20$ G) for a single NV defect coupled with a single ^{13}C nuclear spin belonging to family I ($\mathcal{A}_C^{hs} = 1.12$ MHz). (b) Zoom on the hyperfine transitions associated with a ^{14}N nuclear-spin projection $m_{I^{(N)}} = +1$. Forbidden electron-spin transitions (T_{23},T_{14}) appear in the ESR spectrum when the magnetic field magnitude is increased. (c) Energy level structure of the $m_s = 0$ and $m_s = -1$ ground-state manifolds for a ^{14}N nuclear-spin projection $m_{I^{(N)}} = 1$. Solid (resp. dashed) arrows indicate allowed (resp. forbidden) electron-spin transitions. All notations are defined in the main text.

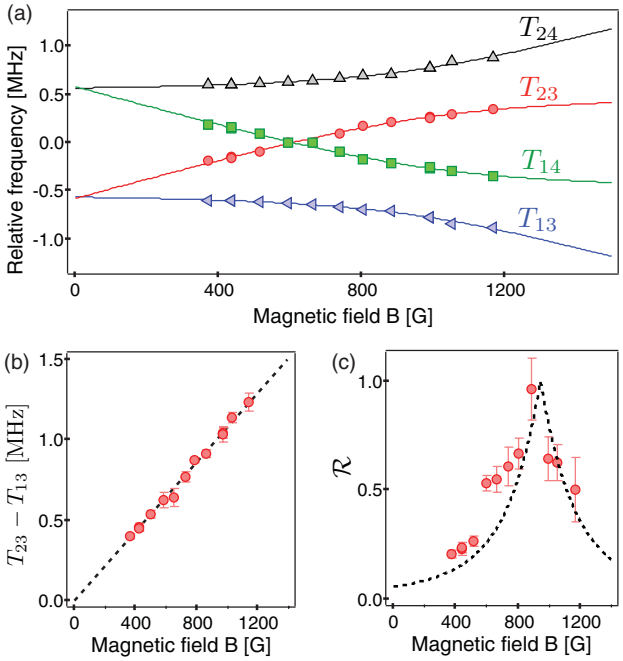

FIG. 4. (Color online) (a) Frequencies of forbidden (T_{23},T_{14}) and allowed (T_{13},T_{24}) electron-spin transitions as a function of the magnetic field magnitude. Solid lines are data fits using Eqs. (12)–(15) with $\mathcal{A}_{zz}$ and $\mathcal{A}_{nd}$ as fitting parameters. (b) $T_{23} - T_{13}$ as a function of the magnetic field magnitude. The black dashed line is data fit with a linear function, from which the ^{13}C nuclear-spin gyromagnetic ratio $\gamma_n = 1.07\,(1)$ kHz.G^{-1} is extracted. (c) Relative intensity $\mathcal{R}$ between forbidden and allowed electron-spin transitions as a function of the magnetic field. The dashed line is the theoretical expectation $\mathcal{R} = \tan^2(\frac{\theta}{2})$, where θ is defined by Eq. (11) with $\mathcal{A}_{zz} = 1.02$ MHz and $\mathcal{A}_{nd} = 0.51$ MHz. The slight deviation of experimental data points is attributed to an imperfect microwave π-pulse in the pulsed-ESR spectroscopy scheme.

[Fig. 4(b)], which is in perfect agreement with the value inferred from nuclear magnetic resonance measurements.[35]

The relative intensity $\mathcal{R}$ between forbidden and allowed electron-spin transitions was estimated by measuring the ratio between the integral of the ESR line at frequency T_{23} and T_{13} [Fig. 4(c)]. As expected, $\mathcal{R} \approx 1$ when $\mathcal{A}_{zz} = \gamma_n B$, i.e., when $B \approx 950$ G. In this situation, $\theta = \pi/2$ and the ^{13}C nuclear quantization axis is perpendicular to the NV defect axis in the $m_s = -1$ electron-spin manifold. We note that this system provides an efficient Λ-scheme that could be used for coherent population trapping of a single nuclear spin and electromagnetically induced transparency experiments in the microwave domain.[36]

C. Polarization efficiency through optical pumping at the excited-state LAC

Hyperfine interactions with nearby ^{13}C were further investigated by measuring their polarization efficiency at the excited-state LAC, while applying a static magnetic field near 510 G along the NV axis [Fig. 1(a)]. In this configuration, electron-nuclear-spin flip-flops mediated by hyperfine interaction in the excited state can lead to an efficient polarization of nearby nuclear spins in their highest spin projection along the excited-state electron-spin quantization axis (z).[32,37,38] Provided that the nuclear-spin projection along the z axis is identical in the ground state and in the excited state, nuclear-spin polarization is transferred to the ground state by nonradiative intersystem crossing through metastable singlet states responsible for electron-spin polarization.[34] The efficiency of such a process is linked to several parameters. First, the polarization $\mathcal{P}$ is reduced if the nuclear-spin quantization axis differs in the ground and in the excited state, as expected for a hyperfine tensor with different principal axis in the ground and in the excited states.[34] For a nuclear spin that possesses an identical quantization axis, the polarization efficiency is also decreased if this axis is not the same as the electron-spin quantization axis, i.e., if anisotropic components of the hyperfine tensor play a significant role in the nuclear-spin dynamics, as observed in the previous section for ^{13}C of family I.

Since the ^{14}N nuclear-spin quantization axis is parallel to the NV defect axis, perfect polarization is achieved in the $m_{I^{(N)}} = 1$ sublevel through optical pumping at the excited-state LAC.[32,37,38] The ESR spectrum of a single NV defect coupled with a single ^{13}C nuclear spin thus only exhibits two hyperfine lines at the excited-state LAC, associated with the two different

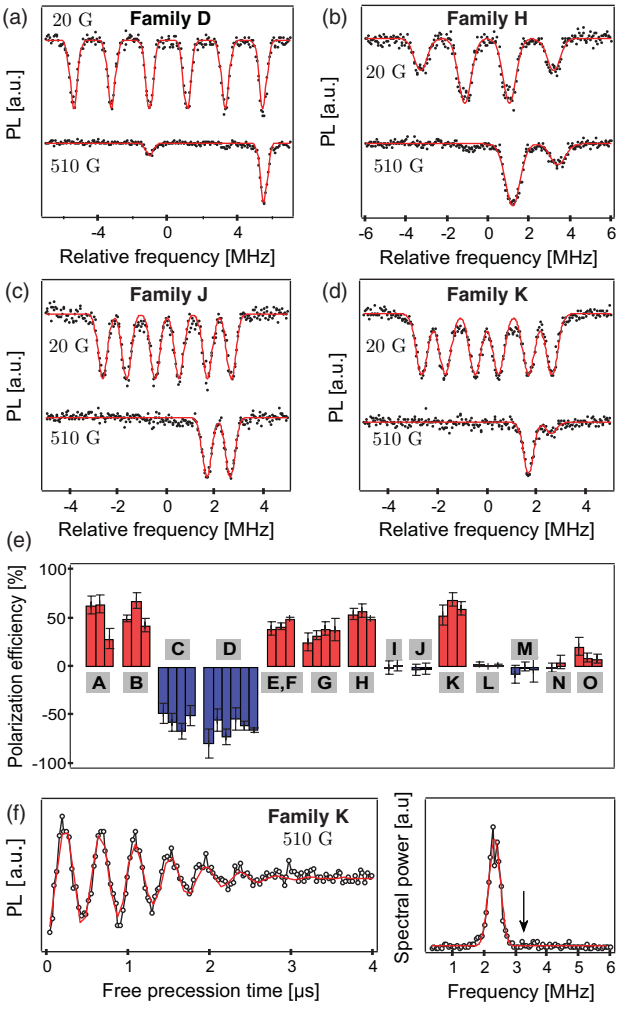

FIG. 5. (Color online) (a)–(d) Typical pulsed-ESR spectra recorded at low magnetic field ($B \approx 20$ G) and at the excited-state LAC ($B \approx 510$ G) for single NV defects coupled by hyperfine interaction with a single ^{13}C belonging to family (a) D, (b) H, (c) J, and (d) K. The ^{14}N nuclear spin is perfectly polarized while the polarization efficiency of nearby ^{13}C strongly depends on the lattice site. (e) Polarization efficiency of a set of single NV defects coupled with different families of ^{13}C. We note that these results are obtained by using pulsed-ESR spectroscopy, i.e., with an optical pumping duration of 300 ns. Positive polarization (resp. negative) indicates a positive (resp. negative) hyperfine splitting. Within each ^{13}C family, the variation of polarization efficiency is attributed to misalignment of the magnetic field along the NV defect axis. The mean polarization efficiency for each ^{13}C family in given in Table I. (f) Free induction decay recorded for the same NV defect as in (d) at the excited-state LAC and for an optical pumping duration of 3 μs. A single line is observed in the Fourier transform, which is the signature of nearly perfect polarization of the ^{13}C nuclear spin.

^{13}C nuclear-spin projections [Figs. 1(b) and 5(a)–5(d)]. For each family of ^{13}C, the polarization efficiency $\mathcal{P}$ was measured as the difference between the integral of each ^{13}C hyperfine line divided by their sum. We note that the amplitude of ESR dips is also affected by the difference in electron-spin readout contrast for the two ^{13}C nuclear-spin orientations when spin flip-flop processes occur in the excited state.[32]

Since all possible ^{13}C lattice sites have different hyperfine interactions with the NV electron spin, each ^{13}C family exhibits different polarization behavior [Figs. 5(a)–5(e)]. For hyperfine splittings larger than 2 MHz (families A to H), only partial nuclear-spin polarization is achieved, which qualitatively demonstrates that the nuclear-spin quantization axis might differ in the ground and in the excited state, as predicted by *ab initio* calculations.[33,34] In addition, the nuclear-spin quantization axis is not the same as the electron-spin axis because none of these ^{13}C families correspond to a lattice site along the NV defect axis.[23] Beyond documenting qualitatively the relative orientation of the ^{13}C, nuclear-spin polarization measurements also indicate the sign of the hyperfine coupling. Indeed, nuclear-spin polarization into the lowest (resp. highest) ^{13}C hyperfine frequency indicates that the hyperfine splitting is positive (resp. negative), which corresponds to a lattice site where the NV defect electron-spin density is positive (resp. negative) [Figs. 5(a) and 5(b)].

For ^{13}C with a hyperfine splitting smaller than 2 MHz [Figs. 5(c) and 5(e)], almost no polarization is observed, except for family K for which a high level of polarization ($\approx$60%) is evidenced in pulsed-ESR spectra [Fig. 5(d)]. However, for such a weak hyperfine interaction (0.95 MHz), the polarization efficiency can be limited by the optical pumping duration, since the probability of electron-nuclear-spin flip-flop per optical cycle is given by the strength of the excited-state hyperfine interaction. In the pulsed-ESR spectroscopy scheme, the optical pumping duration is set at 300 ns in order to optimize the ESR contrast,[31] which could be too short to reach the steady state of nuclear-spin populations. In order to check if nuclear-spin polarization can be improved while increasing the optical pumping duration, the polarization efficiency was estimated by using the Fourier transform of free-induction decay (FID) measurements. For that purpose, Ramsey fringes were recorded by using the standard sequence consisting of a 3-μs laser pulse, used both for optical pumping and spin-state readout, followed by two microwave $\pi/2$-pulses separated by a variable free evolution duration τ. A typical FID signal recorded at the excited-state LAC for a single NV defect coupled with a ^{13}C belonging to family K is shown in Fig. 5(f). The Fourier transform of the FID shows a single line, which is the signature that the ^{13}C nuclear spin is fully polarized. This result might indicate that (i) the hyperfine tensor has an identical principal axis in the ground state and in the excited state, and (ii) that the nuclear-spin quantization axis is parallel to the electron spin. Family K could thus correspond to a ^{13}C placed on a lattice site along the NV defect axis, which shares the symmetry of the NV defect. Such ^{13}C could be an interesting candidate for extending single shot readout measurements recently observed on the ^{14}N nuclear spin at room temperature.[21]

IV. CONCLUSION

Using pulsed-ESR spectroscopy, we have reported a systematic study of the hyperfine interaction between the electron spin of a single NV defect in diamond and nearby ^{13}C nuclear spins. We have isolated a set of discrete values of the hyperfine coupling strength ranging from 14 to 400 kHz and corresponding to ^{13}C nuclear spins placed at different lattice

sites of the diamond matrix. Nuclear-spin polarization measurements suggest that one of the reported hyperfine splittings corresponds to a ^{13}C placed on a lattice site along the NV defect axis. This work provides important information for the development of nuclear-spin-based quantum registers in diamond. In addition, the set of ^{13}C hyperfine splittings combined with their polarization behaviors, can be used for checking *ab initio* calculations of the NV defect spin density.[23,33]

ACKNOWLEDGMENTS

The authors acknowledge L. Childress, P. Bertet, R. Hanson, and F. Jelezko for fruitful discussions. This work was supported by C'Nano Île-de-France and the Agence Nationale de la Recherche (ANR) through the projects DIAMAG, ADVICE and QINVC. J.R.M. acknowledges support from Conicyt Fondecyt, Grant No. 11100265.

*vjacques@lpqm.ens-cachan.fr

[1] F. Jelezko, T. Gaebel, I. Popa, M. Domhan, A. Gruber, and J. Wrachtrup, Phys. Rev. Lett. **93**, 130501 (2004).

[2] M. V. Gurudev Dutt, L. Childress, L. Jiang, E. Togan, J. Maze, F. Jelezko, A. S. Zibrov, P. R. Hemmer, and M. D. Lukin, Science **316**, 1312 (2007).

[3] G. D. Fuchs, G. Burkard, P. V. Klimov, and D. D. Awschalom, Nat. Phys. **7**, 789 (2011).

[4] L. Robledo, L. Childress, H. Bernien, B. Hensen, P. F. A. Alkemade, and R. Hanson, Nature (London) **477**, 574 (2011).

[5] P. Neumann, N. Mizuochi, F. Rempp, P. Hemmer, H. Watanabe, S. Yamasaki, V. Jacques, T. Gaebel, F. Jelezko, and J. Wrachtrup, Science **320**, 1326 (2008).

[6] T. Babinec, M. Khan, Y. Zhang, J. Maze, P. R. Hemmer, and M. Loncar, Nat. Nano. **5**, 195 (2010).

[7] J. Riedrich-Möller, L. Kipfstuhl, C. Hepp, E. Neu, C. Pauly, F. Mücklich, A. Baur, M. Wandt, S. Wolff, M. Fischer, S. Gsell, M. Schreck, and C. Becher, Nat. Nano. **7**, 69 (2012).

[8] A. Faraon, P. E. Barclay, C. Santori, K.-M. C. Fu, and R. G. Beausoleil, Nature Photonics **5**, 301 (2011).

[9] X. Zhu, S. Saito, A. Kemp, K. Kakuyanagi, S. Karimoto, H. Nakano, W. J. Munro, Y. Tokura, M. S. Everitt, K. Nemoto, M. Kasu, N. Mizuochi, and K. Semba, Nature (London) **478**, 221 (2011).

[10] Y. Kubo, C. Grezes, A. Dewes, T. Umeda, J. Isoya, H. Sumiya, N. Morishita, H. Abe, S. Onoda, T. Ohshima, V. Jacques, A. Dréau, J.-F. Roch, I. Diniz, A. Auffeves, D. Vion, D. Esteve, and P. Bertet, Phys. Rev. Lett. **107**, 220501 (2011).

[11] O. Arcizet, V. Jacques, A. Siria, P. Poncharal, P. Vincent, and S. Seidelin, Nat. Phys. **7**, 879 (2011).

[12] G. Balasubramanian, I. Y. Chan, R. Kolesov, M. Al-Hmoud, J. Tisler, C. Shin, C. Kim, A. Wojcik, P. R. Hemmer, A. Krueger, T. Hanke, A. Leitenstorfer, R. Bratschitsch, F. Jelezko, and J. Wrachtrup, Nature (London) **455**, 648 (2008).

[13] J. R. Maze, P. L. Stanwix, J. S. Hodges, S. Hong, J. M. Taylor, P. Cappellaro, L. Jiang, M. V. Gurudev Dutt, E. Togan, A. S. Zibrov, A. Yacoby, R. L. Walsworth, and M. D. Lukin, Nature (London) **455**, 644 (2008).

[14] P. Maletinsky, S. Hong, M. S. Grinolds, B. Hausmann, M. D. Lukin, R.-L. Walsworth, M. Loncar, and A. Yacoby, Nature Nanotechnology, doi: 10.1038/nnano.2012.50.

[15] L. Rondin, J.-P. Tetienne, P. Spinicelli, C. Dal Savio, K. Karrai, G. Dantelle, A. Thiaville, S. Rohart, J.-F. Roch, and V. Jacques, Appl. Phys. Lett. **100**, 153118 (2012).

[16] L. P. McGuinness, Y. Yan, A. Stacey, D. A. Simpson, L. T. Hall, D. Maclaurin, S. Prawer, P. Mulvaney, J. Wrachtrup, F. Caruso, R. E. Scholten, and L. C. L. Hollenberg, Nat. Nano. **6**, 358 (2011).

[17] A. Alhaddad, M.-P. Adam, J. Botsoa, G. Dantelle, S. Perruchas, T. Gacoin, C. Mansuy, S. Lavielle, C. Malvy, F. Treussart, and J.-R. Bertrand, Small **7**, 3087 (2011).

[18] G. Balasubramanian, P. Neumann, D. Twitchen, M. Markham, R. Kolesov, N. Mizuoschi, J. Isoya, J. Achard, J. Beck, J. Tissler, V. Jacques, P. R. Hemmer, F. Jelezko, and J. Wrachtrup, Nat. Mater. **8**, 383 (2009).

[19] N. Mizuochi, P. Neumann, F. Rempp, J. Beck, V. Jacques, P. Siyushev, K. Nakamura, D. J. Twitchen, H. Watanabe, S. Yamasaki, F. Jelezko, and J. Wrachtrup, Phys. Rev. B **80**, 041201(R) (2009).

[20] S. Felton, A. M. Edmonds, M. E. Newton, P. M. Martineau, D. Fisher, D. J. Twitchen, and J. M. Baker, Phys. Rev. B **79**, 075203 (2009).

[21] P. Neumann, J. Beck, M. Steiner, F. Rempp, H. Fedder, P. R. Hemmer, J. Wrachtrup, and F. Jelezko, Science **329**, 542 (2010).

[22] J. H. N. Loubser and J. P. van Wyk, *Diamond Research (London)* (Industrial Diamond Information Bureau, London, 1977).

[23] B. Smeltzer, L. Childress, and A. Gali, New J. Phys. **13**, 025021 (2011).

[24] N. B. Manson, J. P. Harrison, and M. J. Sellars, Phys. Rev. B **74**, 104303 (2006).

[25] J. R. Maze, A. Gali, E. Togan, Y. Chu, A. Trifonov, E. Kaxiras, and M. D. Lukin, New J. Phys. **13**, 025025 (2011).

[26] A. Gruber, A. Dräbenstedt, C. Tietz, L. Fleury, J. Wrachtrup, and C. von Borczyskowski, Science **276**, 2012 (1997).

[27] L. J. Rogers, R. L. McMurtrie, M. J. Sellars, and N. B. Manson, New J. Phys. **11**, 063007 (2009).

[28] A. Batalov, V. Jacques, F. Kaiser, P. Siyushev, P. Neumann, L. J. Rogers, R. L. McMurtrie, N. B. Manson, F. Jelezko, and J. Wrachtrup, Phys. Rev. Lett. **102**, 195506 (2009).

[29] G. D. Fuchs, V. V. Dobrovitski, R. Hanson, A. Batra, C. D. Weis, T. Schenkel, and D. D. Awschalom, Phys. Rev. Lett. **101**, 117601 (2008).

[30] P. Neumann, R. Kolesov, V. Jacques, J. Beck, J. Tisler, A. Batalov, L. Rogers, N. B. Manson, G. Balasubramanian, F. Jelezko, and J. Wrachtrup, New J. Phys. **11**, 013017 (2009).

[31] A. Dréau, M. Lesik, L. Rondin, P. Spinicelli, O. Arcizet, J.-F. Roch, and V. Jacques, Phys. Rev. B **84**, 195204 (2011).

[32] M. Steiner, P. Neumann, J. Beck, F. Jelezko, and J. Wrachtrup, Phys. Rev. B **81**, 035205 (2010).

[33] A. Gali, M. Fyta, and E. Kaxiras, Phys. Rev. B **77**, 155206 (2008).

[34] A. Gali, Phys. Rev. B **80**, 241204(R) (2009).

[35] M. A. Bernstein, K. F. King, and X. J. Zhou, *Handbook of MRI Pulse Sequences* (Elsevier Academic Press, San Diego, 2004).

[36] E. Togan, Y. Chu, A. Imamoglu, and M. D. Lukin, Nature (London) **478**, 497 (2011).

[37] V. Jacques, P. Neumann, J. Beck, M. Markham, D. J. Twitchen, J. Meijer, F. Kaiser, G. Balasubramanian, F. Jelezko, and J. Wrachtrup, Phys. Rev. Lett. **102**, 057403 (2009).

[38] B. Smeltzer, J. McIntyre, and L. Childress, Phys. Rev. A **80**, 050302 (2009).